24

Numerical Simulation for Intranasal Transport Phenomena

Takahisa Yamamoto[1], Seiichi Nakata[2], Tsutomu Nakashima[3] and Tsuyoshi Yamamoto[4]

[1]*Gifu National College of Technology*
[2]*Fujita Health University*
[3]*Nagoya University*
[4]*Kyushu University*
Japan

1. Introduction

More than 10 million people in Japan suffer some of nasal diseases every year (Haruna (2003)); the paranasal sinusitis (so-called the empyema), hypertrophic rhinitis and inferior concha inflammation. Nebulizer treatment has been used for the nasal diseases. The effectiveness of the nebulizer treatment has been confirmed from clinical view points until now. However there are a few researches that evaluate the effect of the nebulizer treatment theoretically and quantitatively, i.e., the transport characteristics of medicinal droplets and their deposition on the inflammation areas of nasal wall.

The development of medical image processing technique is in progress and now gives us exquisitely detailed anatomic information. Some researchers calculated blood flow inside vital arteries and intranasal airflow characteristics by means of the medical image processing technique as well as Computed Fluid Dynamics (CFD) analysis. As for the CFD analysis of intranasal flow, Weinhold et al. constructed both a transparent resin model and numerical three-dimensional anatomy model with nasal cavities using a patient's CT data (Weinhold & Mlynski (2004)). They subsequently made clear airflow characteristics in the nose experimentally and numerically, and found that pressure drop was a main factor of nasal airflow. Lindemann et al. focused at a case which underwent radical sinus surgery (Lindemann et al. (2004; 2005)). In their case, both the lateral nasal wall and the turbinates, inhibiting physiological airflow, were removed by the surgery to realize the enlargements of the nasal cavity volumes and to increase the ratio between nasal cavity volume and surface area. However the researches mentioned here dealt with only a few patient-cases even though there are individual differences in the shape of human nasal cavity and in the grade of medical conditions. The past researches considered the individual differences insufficiently. The authors analyzed intranasal transport phenomena for several patient cases and compared each others in the past study (Monya et al. (2009); Yamamoto et al. (2009)). From the results characteristics of airflow and medicinal droplet transportation strongly depend on inflow conditions such as inflow angle, velocity and size of particle even if there are the individual differences for the shape of patient's nasal cavity.

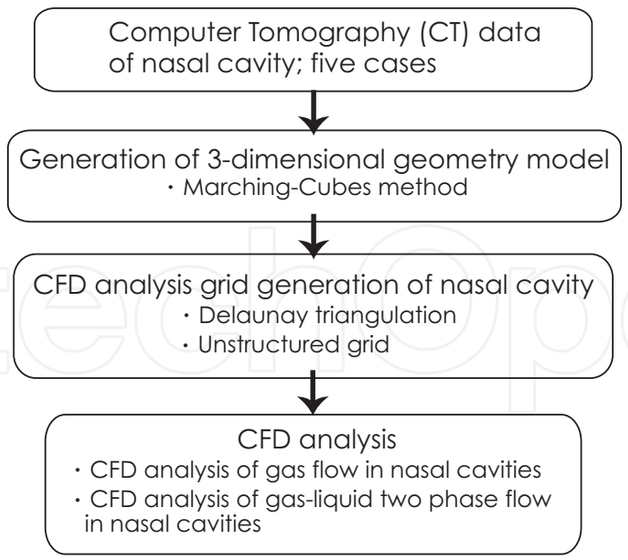

Fig. 1. Flowchart diagram of CFD analysis for heat and mass transport phenomena in nasal cavity

Figure 1 indicates the flowchart of the CFD analysis for intranasal transport phenomena. This chapter shows you detail features of nasal cavity and some nasal diseases, subsequently how to yield three-dimensional model of nasal cavity and calculation mesh for CFD analysis. Finally the characteristics of intranasal transport phenomena are presented in this chapter.

2. Anatomy of nasal cavity

2.1 Structure of nasal cavity and nasal sinuses

Figure 2 shows front and side views of human head, nasal cavity, nasal conchae and nasal sinuses. The nasal cavity is a large air filled space, and the pathway of respiration flow. The nasal cavity conditions the air to be received by the other areas of the respiratory tract. The nasal conchae, which has large surface area, warms and cools passing air through the nasal cavity. At the same time, the passing air is humidified and cleaned by nasal conchae and nasal hairs; most parts of dusts and particulate matters are removed there. The nasal sinuses are four caviums existing in the ossa faciei as shown in Fig.2; maxillary sinus, frontal sinus, ethmoidal sinus and sphenoidal sinus. These sinuses connect to the nasal cavity via very small ducts, ostia; both diameter and streamwise scales are several millimeters. Figures 3 represents coronal and sagittal cross-sectional CT data for nasal cavity and nasal sinuses. The white areas in the figure represent bones of the patient's head, and the gray areas indicate muscles and fat. The nasal cavity and sinuses are represented as dark area in the CT data.
In paranasal sinusitis, both the sinuses and the ostia are infected by bacillus and the virus. The details of such the diseases are stated in following subsections.

2.2 Nasal diseases

The nose often suffers some injuries such as fractures because the nose is protruded forward from the human face. Infection, epistaxis, as well as polyps are also found in the nasal diseases. Almost all people have contract rhinitis which is caused by the inflammation of nasal mucosa. Sinusitis will develop when the inflammation of the rhinitis spread to the sinuses via ostia.

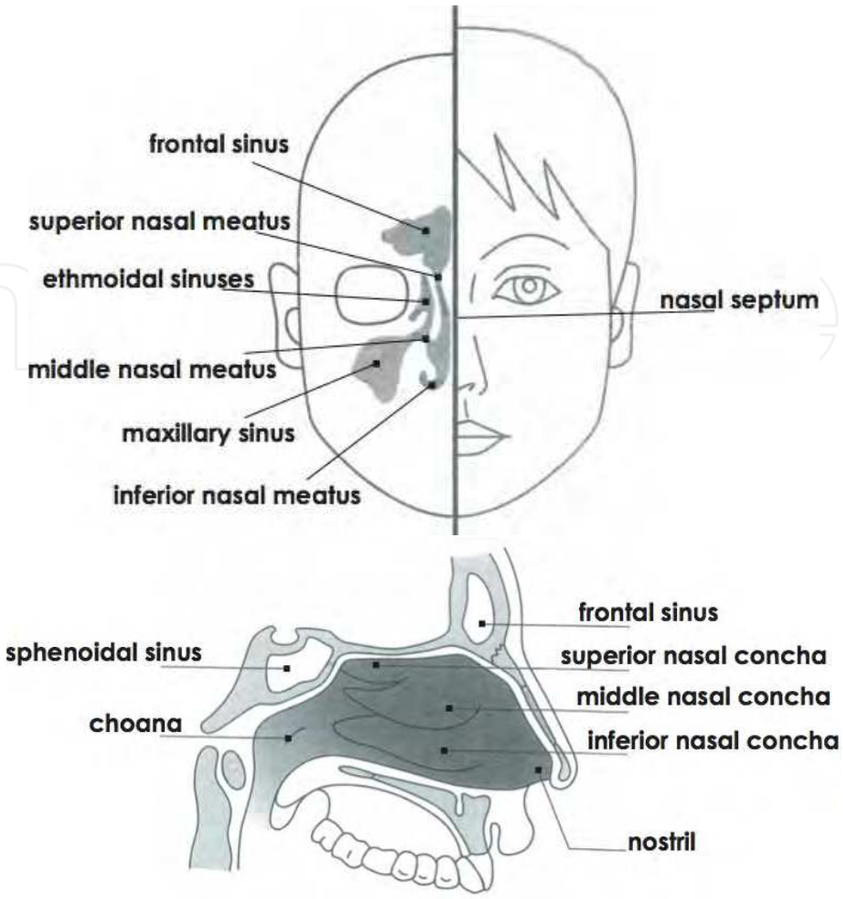

Fig. 2. Front and side view of human head and nasal sinuses (adapted from Haruna (2003))

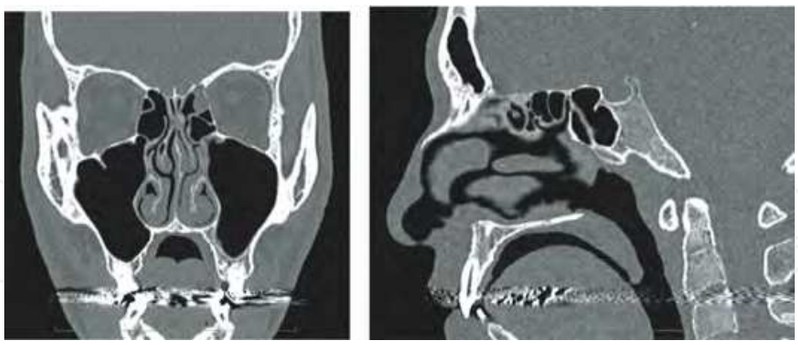

Fig. 3. Cross-sectional CT data for nasal cavity and nasal sinuses: lett) coronal and right) sagittal sections

2.2.1 Deviated nasal septum

Nasal septum locates on the middle of left and right nasal cavities, being almost straight stretches. Many people has a slightly-curved nasal septum as shown in the left-side figure of Fig.5. There are small size different between the left and right nostrils. The right figure of Fig.5 indicates a CT image that is the case of deviated nasal septum. The deviated nasal septum is caused by external nasal injuries and/or congenital origin. As for the cases, one of the nasal

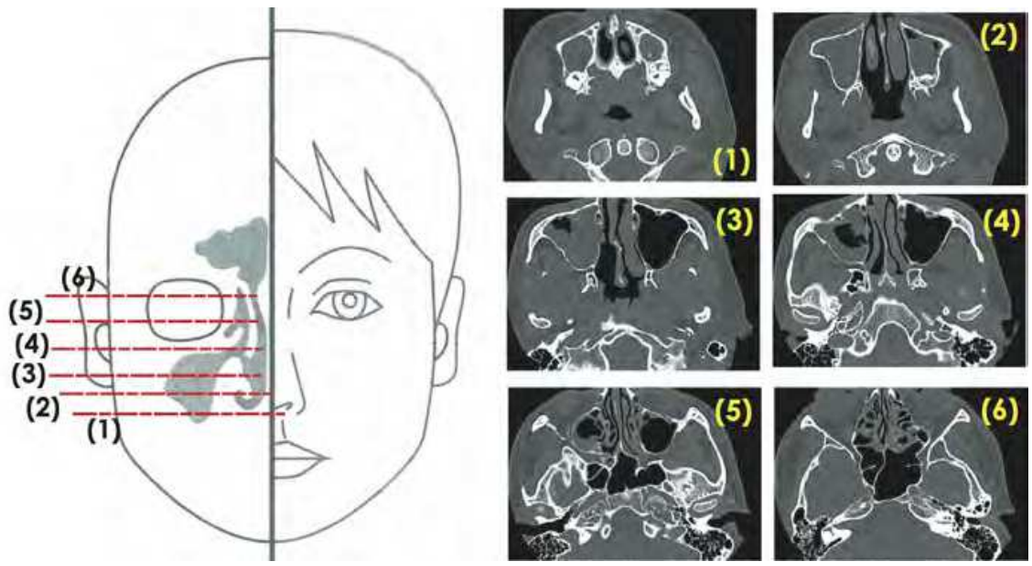

Fig. 4. Series of axial cross-sectional CT data for nasal cavity and nasal sinuses (adapted from Haruna (2003))

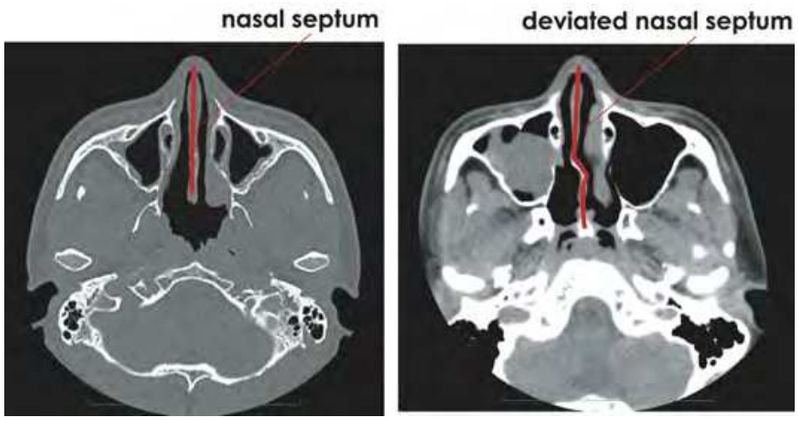

Fig. 5. Axial cross-sectional CT data for nasal septum: left) healthy nasal septum and right) deviated nasal septum

cavity is significantly smaller than the other. Then the patient suffers nasal congestion and drying nasal cavity, consequently epistaxis. In the sever cases operative treatment is required.

2.2.2 Rhinitis (nasal inflammation)

The nasal cavity is the part that easily causes infection in the upper respiratory tracts. Rhinitis (nasal inflammation) is mainly classified into two cases; the one is acute rhinitis and the other is chronic rhinitis. The acute rhinitis is generally caused by the infection of virus and allergies of pollen and house dust. The difference point between both rhinitis is the term of these diseases; the former occurs in a short term and the latter in a long term (two weeks and more). In some cases, the chronic rhinitis occasionally accompanies the chronic sinusitis.

2.2.3 Sinusitis

Figure 6 shows cross-sectional CT data for both healthy maxillary sinus and sinusitis one. The sinusitis happens anywhere about four kinds of the sinus paranasalis such as the maxillary sinus, sinus ethmoidales, the master wrestlers caves, and the sphenoidal sinuses. The sinusitis is classified into the acute sinusitis (in a short term) and the chronic sinusitis (in a long term).

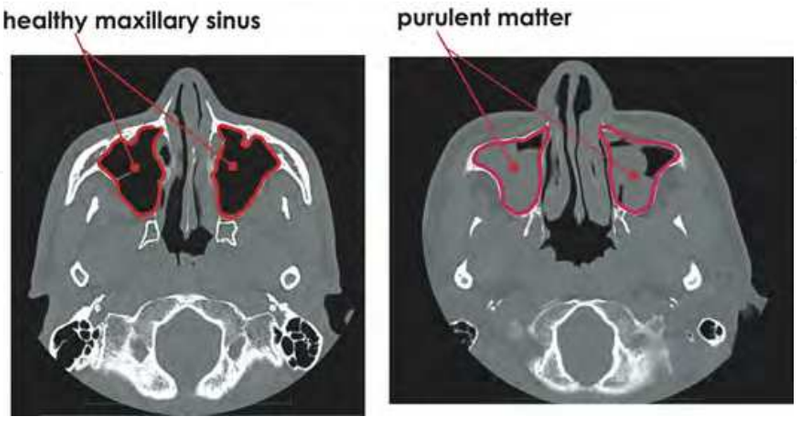

Fig. 6. Cross-sectional CT data for maxillary sinuses: left) healthy maxillary sinus and right) sinusitis

The acute sinusitis is caused by a variety of bacteria and virus, often develops after the blockage of ostia which are opening of sinuses connecting to nasal cavity. The blockage normally occures as a result of virus infection in the upper respiratory caused by a cold. The cold brings on the swelling of the mucous membrane of nostril, and then the ostia are easily obstructed. In the blocked sinus, the air inside the cavity are absorbed to the bloodstream, and subsequently the pressure inside the sinus decreases. This pressure drop produce sever pains and the sinus fills with secretory fluid. The secretory fluid becomes a breeding ground for viruses. In order to attack the viruses, white blood cell and other matters such as the secretory fluid are aggregated in the blocked sinus, then the pressure in the sinus is increased and pain becomes more sever.

The case that a symptom of the sinusitis continues more than 8-12 weeks is called the chronic sinusitis. The developing mechanism of the chronic sinusitis has not been clear, however it has been confirmed that the chronic sinusitis develops after the infection of the virus, severe allergies and the influences of the environmental pollution material. A genetic contributor is also regarded as one of the factors concerned with development of the chronic sinusitis.

3. Construction of three-dimensional nasal cavity model

In order to construct a three-dimensional model for nasal cavity, data conversion algorithm from two-dimensional CT/MRI data to three-dimensional geometric model as well as smoothing algorithm for the three-dimensional model are required. Furthermore, mesh generation models are needed to execute CFD analysis of intranasal transport phenomena. This section describes the fundamental theories of these algorithms.

3.1 Data conversion algorithm from 2-D to 3-D: marching cubes algorithm

Marching cubes algorithm is one of the latest models of surface construction used for viewing three-dimensional data (Lorensen & Cline (1987)). This algorithm extracts a polygonal mesh

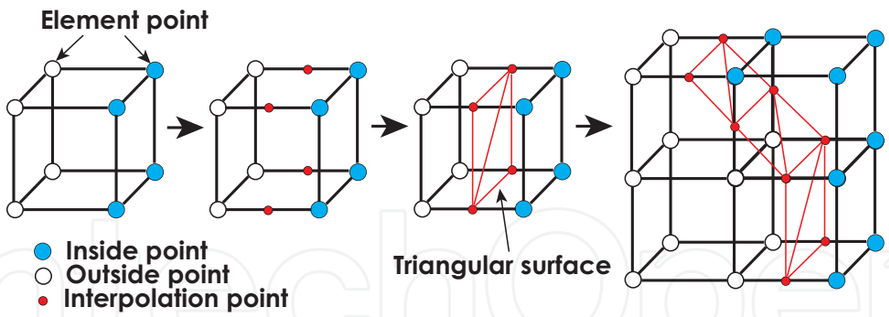

Fig. 7. Configurations of fourteen unique cubes for marching cubes algorithm

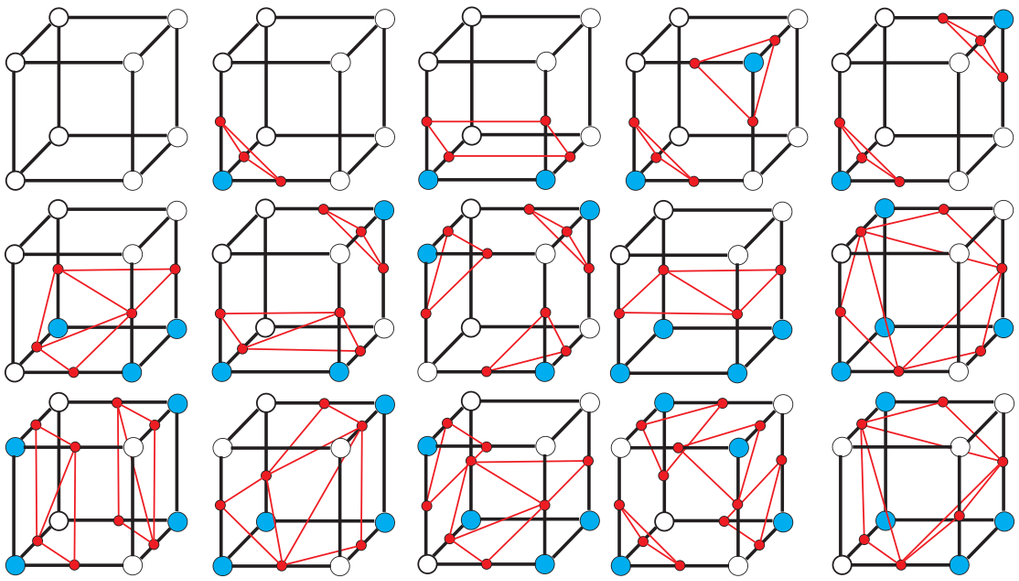

Fig. 8. Triangular surface patterns for the marching cubes algorithm

of isosurface from a three-dimensional scalar field. The algorithm proceeds through the scalar field, taking eight neighbor locations at a time, then determining the polygons needed to represent the part of the isosurface that passes through this cube. The individual polygons are then fused into the desired surface as shown in Fig.7. This is done by creating an index to a pre-calculated array of 256 possible polygon configurations (2^8 = 256) within the cube, by treating each of the 8 scalar values as a bit in an 8-bit integer. Finally each vertex of the generated polygons is placed on the appropriate position along the cube's edge by linearly interpolating the two scalar values that are connected by that edge. The precalculated array of 256 cube configurations can be obtained by reflections and symmetrical rotations of 14 unique cases as shown in Fig.8.

The applications of this algorithm are mainly concerned with medical visualizations such as CT and MRI scan data images, and special effects on three-dimensional modeling.

3.2 Smoothing algorithm

In the image processing and image transmission, noises are physically captured and fed into the processes due to various factors. For instance, noises are generated caused by the image resolution and image slice thickness of CT and MRI in the field of medical engineering. When the noise generation mechanism is clear and mathematically modeled, we can remove the noise using the optimized filter. However, it is difficult to modeled the noise mathematically in almost all situations.f The smoothing processes are needed to reduce and minimize the influence of the noise. The noise makes patterned indented surfaces in the three-dimensional model, therefore affects the quality of the constructed nasal cavity model significantly. There are two smoothing algorithms that often uses in the medical image processing; moving-average algorithm and median-average algorithm. This subsection presents both algorithms as follows.

3.2.1 Moving-average algorithm

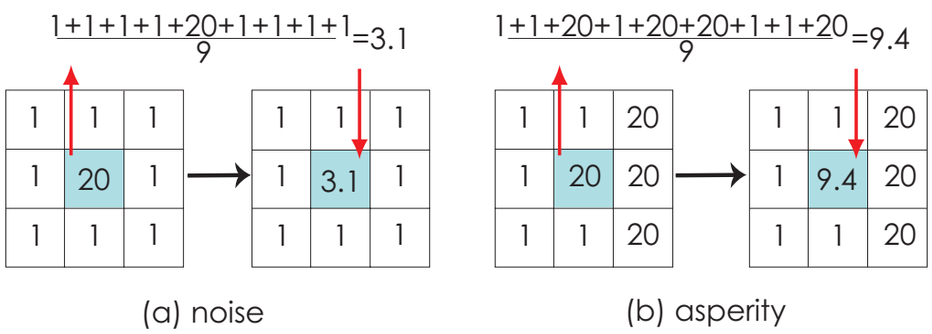

Fig. 9. Procedure of Moving-Avarage Algorithm for 3 × 3 Cubes

Figure 9 shows the application of the moving-average algorithm for 3 × 3 cubes (Savitzky & Golay (1964); Sun (2006); Tamura (2002)). The number inside a cube expresses a scalar variable, for example the concentration of a chemical specie. The case of Fig.9(a) presents a noise included in the data and that of Fig.9(b) expresses an asperity in the data. The moving-average algorithm calculates an average of surroundings of the concentration $f(i,j)$ in the input image, and converts to the concentration $g(i,j)$ in the output image.

$$g(i,j) = \frac{1}{n^2} \sum_{k=-[n/2]}^{n/2} \sum_{l=-[l/2]}^{n/2} f(i+k, j+l) \tag{1}$$

The moving-average algorithm feathers the edge and the boundary of the input image, consequently smoothes the object surfaces.

3.2.2 Median-average algorithm

Figure 10 indicates the application of the median-average algorithm for 3 × 3 cubes (Boyle & Thomas (1988); Tamura (2002)). The cases of Fig.10(a) and (b) represent a noise and an asperity in the data, respectively. This algorithm sorts both a concentration value $f(i,j)$ at a target position of the input image and its surroundings in ascending order, subsequently converts the output image $g(i,j)$ using their median value. As for Fig.10(a), the concentration values in input image are rearranged like "1, 1, 1, 1, 1, 1, 1, 1, 20" in ascending order, and then the fifth value "1" is picked up as a median value and used as the concentration $g(i,j)$ in the

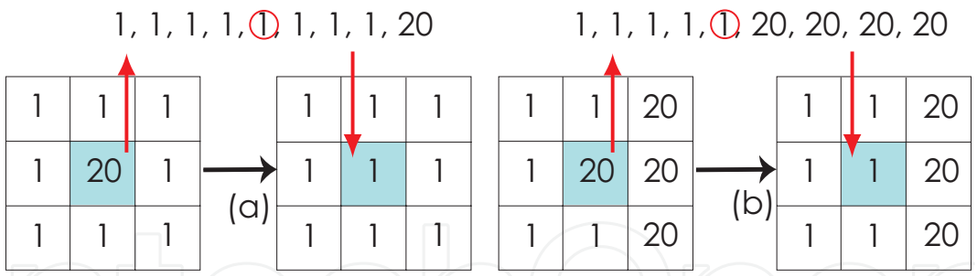

Fig. 10. Procedure of Median-Average algorithm for 3×3 cubes

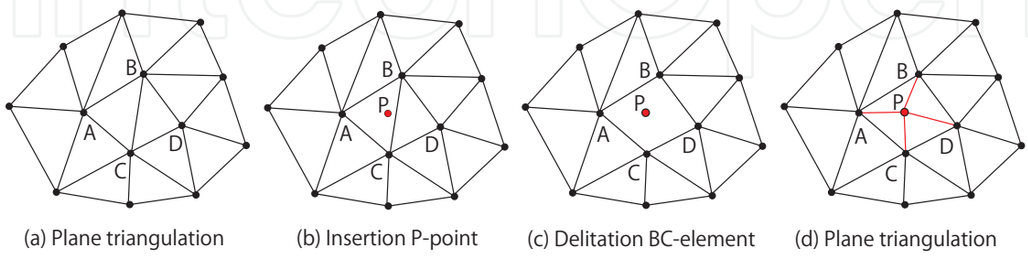

Fig. 11. Schematic drawing of the Delaunay triangulation model

output image. On the other hand, the concentration values in input image are rearranged like "1, 1, 1, 1, 1, 20, 20, 20, 20" in ascending order as shown in Fig.10(b). Finally, the fifth value "1" is selected as the concentration $g(i, j)$ in the output image. The median-average algorithm can remove the noise effectively compared with the moving-average algorithm. At the same time, this algorithm involves a risk that the magnitude of rearranging the original CT/MRI data is larger than the moving-average algorithm, consequently could yield different three-dimensional model from the real target.

3.3 Mesh generation: Delaunay triangulation model

The Delaunay triangulation model is one of the most-used mesh generation technique. This model is applicable for a wide variety of very complicate geometries.

This model mathematically ensures that the circumcircle associated with each triangle contains no other point in its interior. This definition extends naturally to three-dimensional problems. Figure 11 shows a schematic drawing of the Delaunay triangulation model (Nakahashi (1995)). The triangles as shown in Fig.11(a) contains the edges and the edge's endpoints. A new point "P" is added inside the triangle "ABC", then the mathematical theory of the Delaunay triangulation is not satisfied in the triangle "ABC" and its surrounding triangle "BCD". The model can eliminate the edge "BC" which is a common edge for both triangles "ABC" and "BCD", subsequently reconstruct triangles using the added point "P". Consequently, as shown in Fig.11(d), the model can yield four triangles "ABP", "ACP", "BDP" and "CDP". The Delaunay triangulation constructs and reconstructs triangles in target domain simultaneously and give us fine meshes for CFD analysis.

4. Theory of computational fluid dynamics

In the nasal cavity, particulate matters such as pollens, house dust as well as medicinal droplets are transported via airflow of the respiration and the nebulizer treatment. In order

to execute CFD analysis for such the transport phenomena, we have to consider multi-phase flow. This section describes the basic theory of CFD analysis for two-phase flow.

4.1 Governing equations for continuous phase

The Reynolds number of intranasal flow is a few hundred. Therefore the flow is assumed as incompressible and laminar flow.
The equation for conservation of mass, or continuity equation, can be written as follows:

$$\frac{\partial \rho_F}{\partial t} + \nabla \cdot \rho_F \mathbf{u_F} = 0 \tag{2}$$

here ρ_F and $\mathbf{u_F}$ are density and velocity of continuous phase. Equation 2 is the general form of the mass conservation equation and is valid for incompressible as well as compressible flows. Conservation of momentum in an inertial reference frame is described by

$$\frac{\partial \rho_F \mathbf{u_F}}{\partial t} + \mathbf{u_F} \cdot \nabla \rho_F \mathbf{u_F} = -\nabla p + \mu_F \nabla^2 \mathbf{u_F} + \rho_F \mathbf{g} + \mathbf{F} \tag{3}$$

where p is the static pressure, μ_F is viscosity of the fluid, and $\rho\mathbf{g}$ and $\mathbf{F}$ are gravitational body force and external body forces, respectively. $\mathbf{F}$ contains interaction with the dispersed phase in multi-phase flow and other model-dependent source terms.
The thermal energy transport equation is meant to be used for flows which are low speed and close to constant density.

$$\frac{\partial \rho_F c_p T_F}{\partial t} + \mathbf{u_F} \cdot \nabla \rho_F c_p T_F = \nabla \cdot (\lambda_F \nabla T_F) + \mathbf{S_{FP}} \tag{4}$$

where c_p and λ_F are specific heat at constant pressure and heat conductivity, respectively. S_{FP} denotes a source term regarding the interaction between continuous phase and disperse phase.

4.2 Governing equations for disperse phase

Consider a discrete particle traveling in a continuous fluid medium. The forces acting on the particle which affect the particle acceleration are due to the difference in velocity between the particle and fluid, as well as to the displacement of the fluid by the particle. The equation of motion for such a particle was derived by Basset, Boussinesq and Oseen for a rotating reference frame (Akiyama (2002)):

$$m_p^i \frac{d\mathbf{u_p}}{dt} = \mathbf{F^i_{Drag}} + \mathbf{F^i_{Pressure}} + \mathbf{F^i_{Basset}} + \mathbf{F^i_{Buoyancy}} + \mathbf{F^i_{Rotation}} + \mathbf{F^i_{Others}} \tag{5}$$

where, superscript i denote the i-th particle, and $\mathbf{F_{Drag}}$, $\mathbf{F_{Pressure}}$, $\mathbf{F_{Basset}}$, $\mathbf{F_{Buoyancy}}$, $\mathbf{F_{Rotation}}$ express drag force acting on the particle, pressure gradient force, Basset force, buoyancy force due to gravity and forces due to domain rotation, respectively. The pressure gradient force term applies on the particle due to the pressure gradient in the fluid surrounding the particle caused by fluid acceleration. The Basset force term accounts for the deviation in flow pattern from a steady state.
The aerodynamic drag force on a particle is propotional to the slip velocity between the particle and the fluid velocity

$$\mathbf{F^i_{Drag}} = \frac{1}{8}\pi (d^i)^2 \rho_F C_D \mathbf{u_F} - \mathbf{u_P}(\mathbf{u_F} - \mathbf{u^i_P}) \tag{6}$$

where $\mathbf{u_F}$ and $\mathbf{u_P}$ are the velocities of the fluid flow and the particle. C_D denotes the drag coefficient of the particle.

$$C_D = \frac{24}{Re^i(1 + 0.15(Re^i)^{0.687})} \tag{7}$$

Re^i is the Reynolds number based on the slip velocity between the fluid flow and the i-th particle velocities.

$$Re^i = \frac{d^i(\mathbf{u_F} - \mathbf{u_P^i})}{\nu_F} \tag{8}$$

The pressure gradient force results from the local fluid pressure gradient around the particle and is defined as

$$\mathbf{F^i_{pressure}} = -\frac{1}{6}\pi(d^i)^3\nabla p \tag{9}$$

This force is only important if large fluid pressure gradients exist and if the particle density is smaller than or similar to the fluid density.

$$\mathbf{F^i_{Basset}} = \frac{3}{2}(d^i)^2\sqrt{\pi\rho_F\mu_F}\int_{t_0}^{t}\frac{d(\mathbf{u_F} - \mathbf{u_p^i})}{d\tau}(t-\tau)^{-\frac{1}{2}}d\tau \tag{10}$$

The buoyancy force is the force on a particle immersed in a fluid. The buoyancy force is equal to the weight of the displaced fluid and is given by

$$\mathbf{F^i_{Buoyancy}} = \frac{3}{2}(d^i)^3(\rho_P^i - \rho_F)\mathbf{g} \tag{11}$$

here $\mathbf{g}$ expresses the gravity vector.
In rotating frame of reference, the rotation term is an intrinsic part of the acceleration in and is the sum ob Coriolis and centripetal forces.

$$\mathbf{F_{rotation}} = -\frac{1}{3}(d^i)^3\rho_P(\omega \times \mathbf{u_P}) - \frac{1}{6}\rho_P\omega \times (\omega \times \mathbf{r_P}) \tag{12}$$

where, ω denotes rotation speed of the reference.
In the intranasal flow and heat and mass transfer, the influence of both the pressure gradient term and the Basset force term on the transport phenomena in the nasal cavity is extremely small. The momentum conservation equation for the particle is shown as

$$m_P^i\frac{d\mathbf{u_P^i}}{dt} = \frac{1}{8}\pi(d^i)^2\rho_F C_D\mathbf{u_F} - \mathbf{u_P^i}(\mathbf{u_F} - \mathbf{u_P^i}) \tag{13}$$

When the Lagrangian method is applied to the particle movement, the location of the particle is given by

$$\frac{d\mathbf{x_P^i}}{dt} = \mathbf{u_P^i} \tag{14}$$

As for the almost all particulate matter transported in nasal cavity, the mass fraction of the disperse phase are extremely small compared with the continuous phase. Therefore it is only necessary to consider the one-way interaction between both phases, namely only the continuous phase influences the disperse phase.
Heat transfer concerning the disperse phase is governed by three physical processes, namely convective heat transfer, latent heat transfer associated with mass transfer, and radiative heat transfer. Since the heat transfer of intranasal flow is not so high temperature condition, we

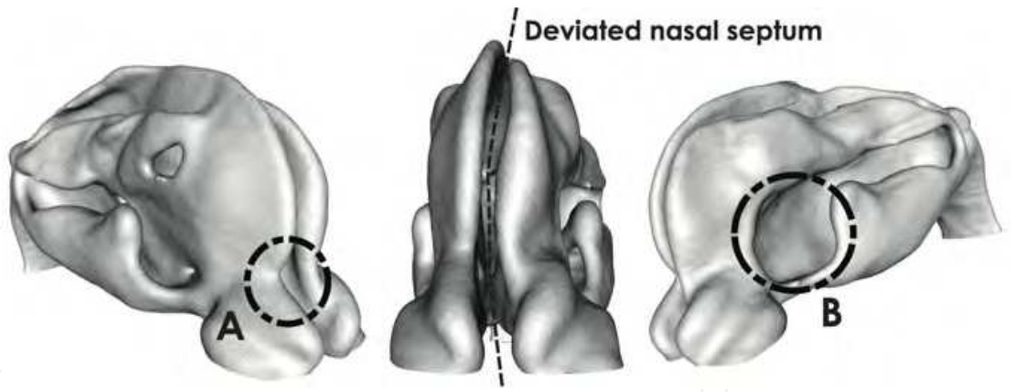

Fig. 12. Three-dimensional nasal cavity model (case-1)

Case No.	Deviated nasal septum	Chronic sinusitis	hypertrophic rhinitis	Bloating inferior concha
1	◯	Left	Left	
2		Left & Right		
3	◯		Left & Right	Left
4	◯		Left & Right	
5	◯		Left & Right	Left

Table 1. Detail patient's case data

can neglect both the latent heat transfer and the radiative heat transfer. The convective heat transfer Q_C is given by

$$Q_C^i = \pi d^i \lambda_F Nu(T_F - T_P^i) \tag{15}$$

where T_P^i is the temperature of the i-th particle, and Nu is the Nusselt number given by

$$Nu = 2 + 0.6Re^{0.5}(\mu_F \frac{C_p}{\lambda_F})^{\frac{1}{3}} \tag{16}$$

The convective heat transfer Q_C is calculated and used in the source term of the thermal energy transport equation, Eq.4.

5. Numerical simulations of intranasal transport phenomena

5.1 Case data and three-dimensional model

Three-dimensional models of nasal cavity were constructed by means of five actual patient's CT data. These cases suffer several grades of deviated nasal septum symptom, hypertrophic rhinitis, chronic sinusitis and inferior nasal concha swelling. The case data are summarized in Table 1. Since head CT data involves not only nasal cavity but also skin, fat, bone and purulent matter, it is required to eliminate them. This study used three-dimensional medical image processing software "Mimics (Materialize Inc.)" and the marching cubes algorithm to determine the surfaces of nasal wall. The moving-average algorithm is also applied to smoothing the surface. Figure 12 shows the three-dimensional nasal model of case-I constructed in this study. The anterior and the posterior of the figure show anterior nares and upper pharynx, respectively. The three-dimension model has curved nasal septum which corresponds to the curvature as shown in Fig.12. The cross-sectional areas of nasal cavities

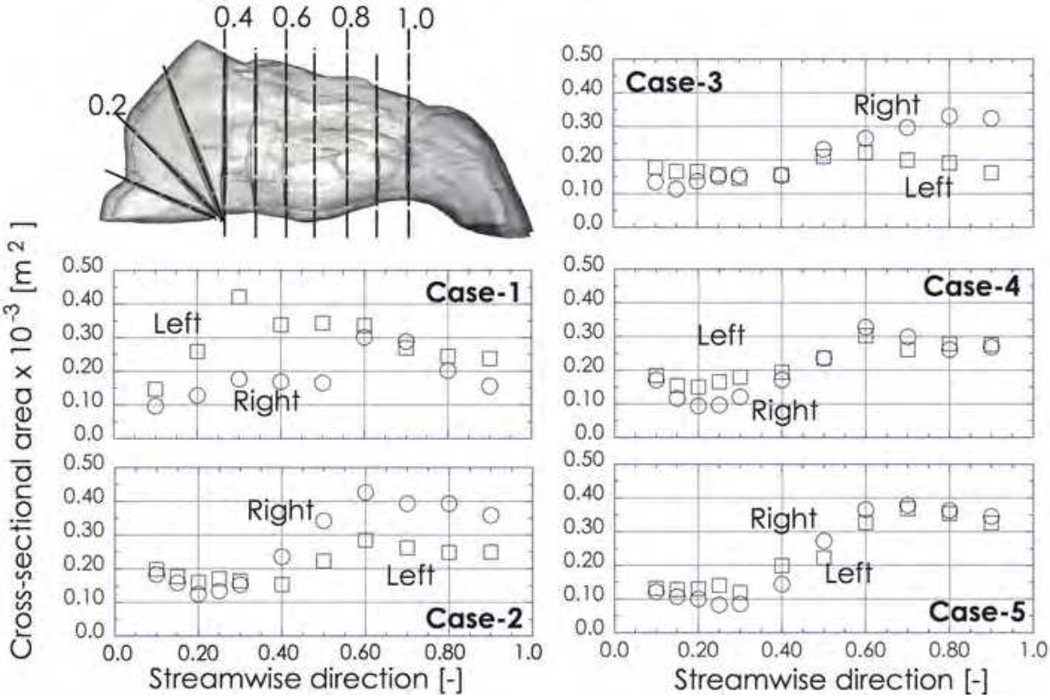

Fig. 13. Summaries of cross-sectional areas of nasal cavities for all cases

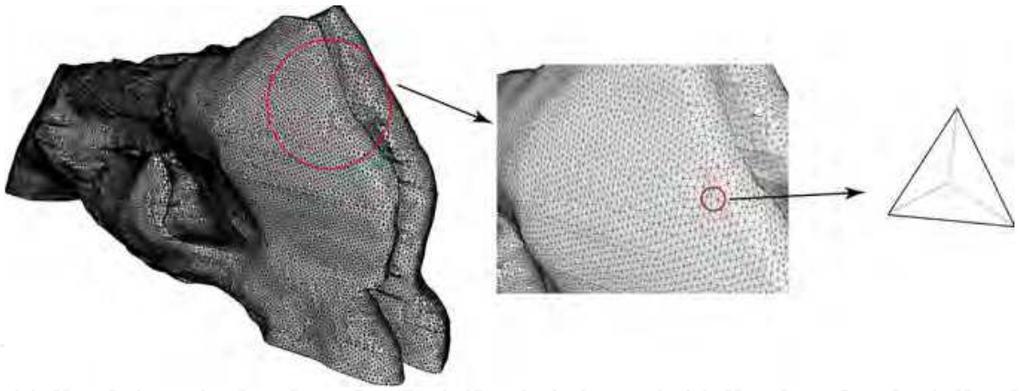

Fig. 14. Schematic drawing of CFD analysis grid (unstructured grid)

which significantly affect intranasal flow are summarized in Fig.13. The lumen and the wall of three-dimensional models are meshed using commercial meshing software ICEM CFD (ANSYS, Inc.) and the delaunay triangulation algorithm as shown in Fig.14.

Figure 15 indicates a example of the influence of the mesh quality on the accuracy of CFD analysis. In this figure, pressure drop between inlet and outlet and the number of grid nodes are used as the factors of the accuracy and the mesh quality, respectively. The pressure drop significantly depends on the number of grid nodes; the pressure drop shows occasional ups and downs in the case of small number of grid nodes, on the contrary it becomes stable in the case of large number of grid nodes.

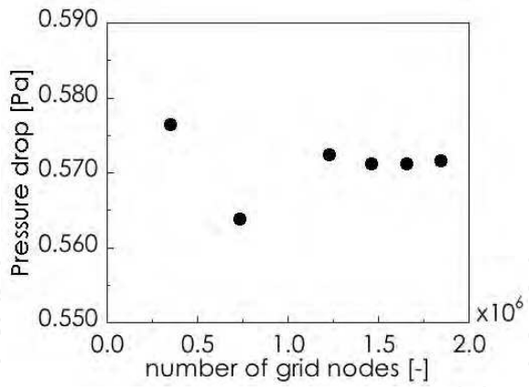

Fig. 15. Dependency between pressure drop and number of grid nodes in the CFD analysis for case-I

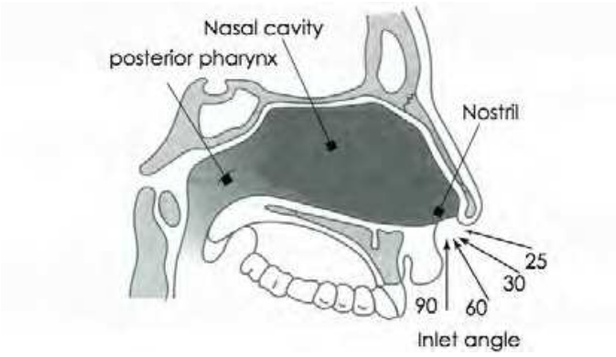

Fig. 16. Schematic figure of inlet nebulizer angles; 90, 60 and 30 degree

5.2 Computational fluid dynamics model

This study used CFD analysis code "CFX-11 (ANSYS, Inc.)" to analyze the intranasal transport phenomena of the nebulizer treatment. This code is able to solve partial differential equations for mass, momentum and energy transportations with appropriate boundary conditions. Since the Reynolds number of intranasal flow was several hundred, normal laminar flow analysis was used in this study. The Lagrange approach is adopted to solve transportation of the droplets of medicinal mist. Then the model employs assumptions that a droplet is sensitive with fluid flow, accelerating by velocity difference between fluid flow and the droplet. Air inlet velocity is set at 0.5m/s. This velocity condition corresponds to the condition of actual nebulizer treatment. As shown in Fig.16, four air inlet angles are considered in this study; 90, 60, 30 and 25 degree. In the nebulizer treatment, medicinal mist is atomized and transported by dry air. This study considers dry air (298K, 0.1MPa) as a fluid medium. No-slip condition, where fluid velocity on the wall surface is set at zero, is adopted to the nasal wall. Droplet diameter of medicinal mist is uniformly 50 micro meters. This value also corresponds to the condition of actual nebulizer treatment.

5.3 Results and discussion

Figures 17-19 shows stream lines in case-I left nasal when inlet velocity is 0.5m/s and nebulizer angles are 90, 60 and 30 degree. As we can see from the stream lines, changing nebulizer angle 60 to 30 degree changes the main flow of nebulizer from the superior nasal concha (upper-area of nasal cavity) to the inferior nasal concha (lower-area). In the all

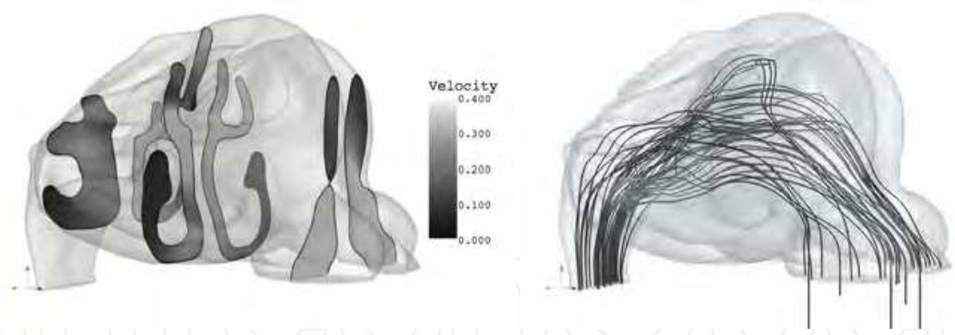

Fig. 17. Results of intranasal flow of the case-I; velocity magnitude distribution in each cross-section and streamlines (inflow velocity of 0.5m/s and inlet angle of 90 degree)

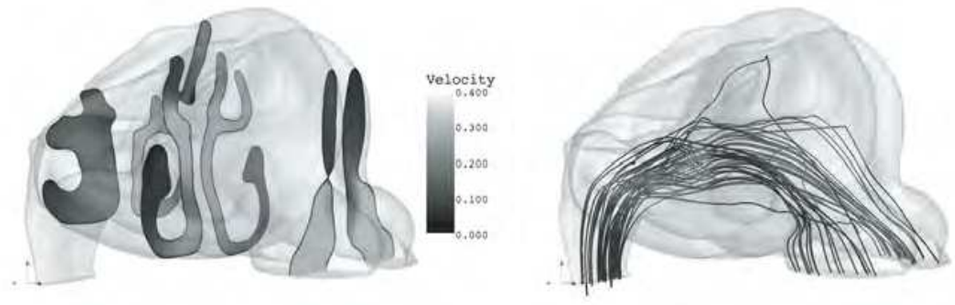

Fig. 18. Results of intranasal flow of the case-I; velocity magnitude distribution in each cross-section and streamlines (inflow velocity of 0.5m/s and inlet angle of 60 degree)

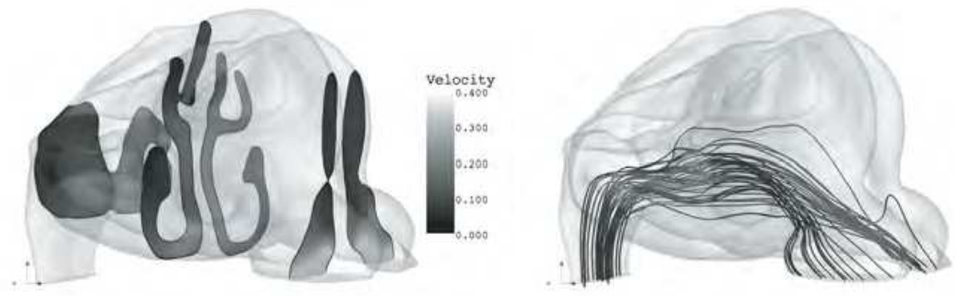

Fig. 19. Results of intranasal flow of the case-I; velocity magnitude distribution in each cross-section and streamlines (inflow velocity of 0.5m/s and inlet angle of 30 degree)

nebulizer angle conditions flow velocity increases near the nares. Especially, the increasing flow velocity is most obvious in the inflammation regions. Circulation flow is found in the lower inlet angle conditions. This circulation flow will be able to extend residence times of airflow and medicinal droplet in nasal cavity, consequently enhance the effect of the nebulizer treatment.

Figure 20-22 shows trajectories of medicinal droplets is the case-III when inlet velocity is 0.5m/s and inlet angles are 90, 60 and 30 degree. Almost all droplets impinge and deposit near the nares and middle nasal concha where the cross-section areas are narrow caused by deviated nasal septum and inflammation. From these results, the nebulizer angle is able to control the impingement and deposition characterisitics of medicinal droplets. By the control

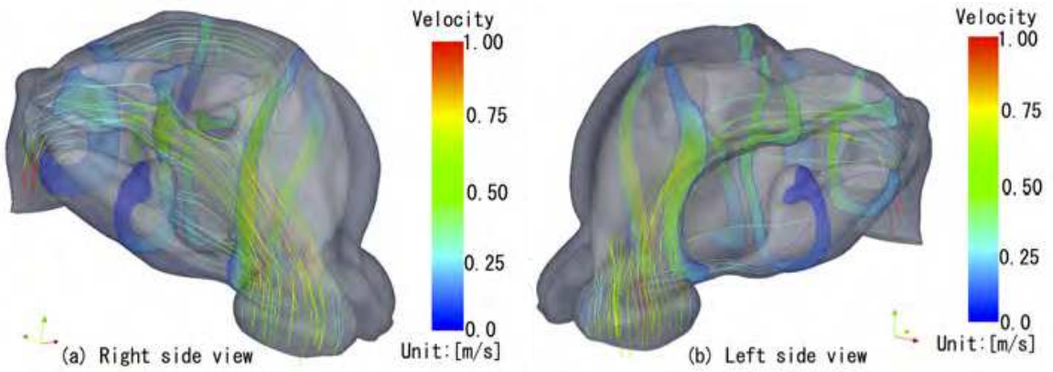

Fig. 20. Trajectories of nebulizer droplets of the case-III; inflow velocity of 0.5m/s and inlet angle of 90 degree)

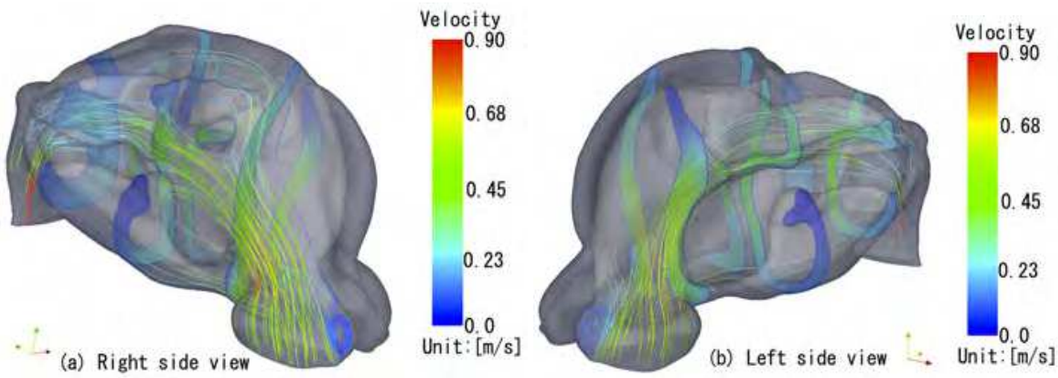

Fig. 21. Trajectories of nebulizer droplets of the case-III; inflow velocity of 0.5m/s and inlet angle of 60 degree)

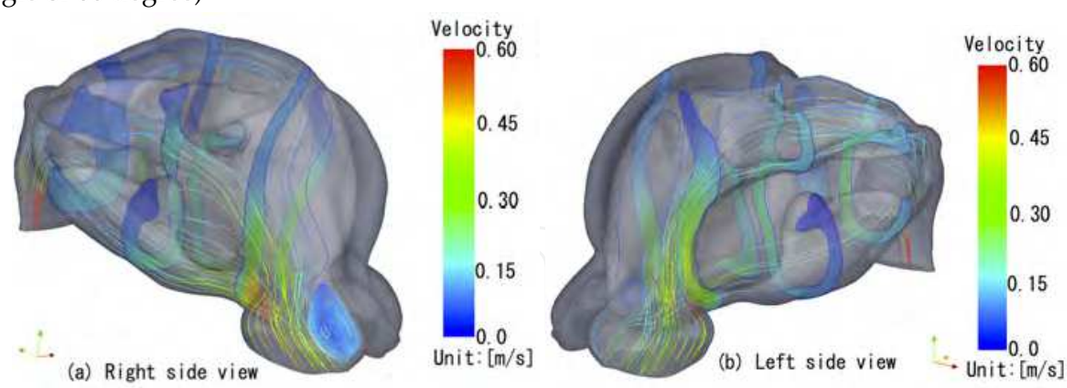

Fig. 22. Trajectories of nebulizer droplets of the case-III; inflow velocity of 0.5m/s and inlet angle of 30 degree)

of nebulizer angle, we can reduce the amount of medicinal droplet's deposition on nares and middle nasal concha, consequently transport wide area of nasal cavity.

This study focuses and uses three parameters to organize the results of each case; pressure drop of nebulizer flow, maximum velocity of intranasal flow and deposition ratio which expresses how many droplets impinge and deposit on nasal wall. Figures 23-25 are correlations among them for all patient's cases. The correlations of each case show similar

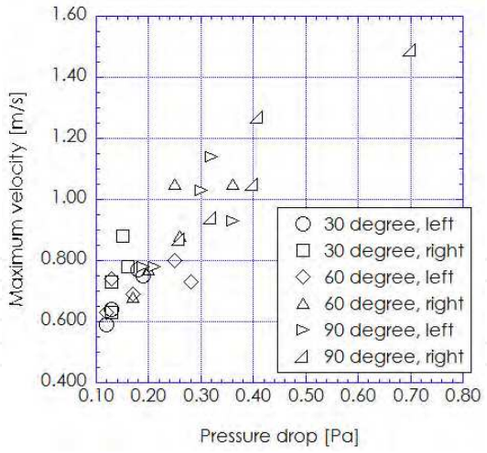

Fig. 23. Correlation analysis between maximum velocity and pressure drop

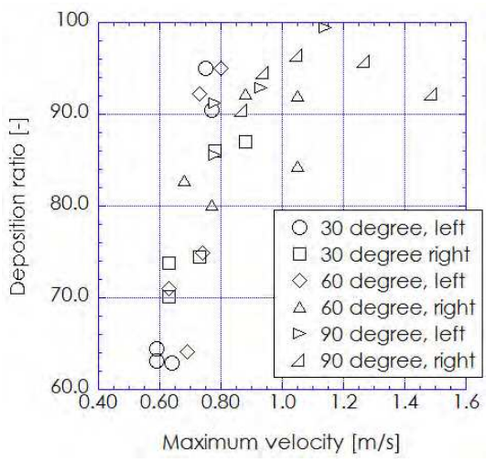

Fig. 24. Correlation analysis between deposition ratio and maximum velocity

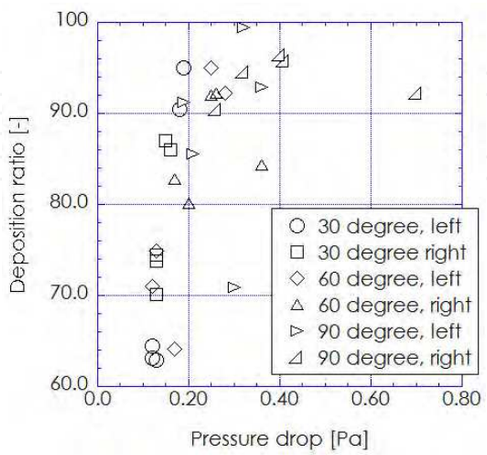

Fig. 25. Correlation analysis between deposition ratio and pressure drop

tendencies even though there are the individual differences such as the shape of nasal cavity and the state of nasal disease. Therefore these parameters are useful to organize the results mentioned above. The maximum velocity has direct proportional relationship with pressure drop. Meanwhile pressure drop and maximum velocity have strong correlation with deposition ratio. These results lead us to conclude that the nebulizer conditions have same-level influence on the intranasal transport phenomena for all cases.

6. Conclusion

This chapter presents not only the procedure of CFD analysis for intranasal transport phenomena but also medicinal droplets transport characteristic in patient's nasal cavity using actual CT/MRI data. Furthermore, the result of correlation analysis for the nebulizer treatment condition is also presented here. As for the results of CFD analysis, nebulizer angle, inlet velocity and size of droplet significantly affect on the intranasal transport phenomena. The condition of low nebulizer angle achieves that the medicinal droplets are transported all over the nasal cavity, that is this condition will increases therapeutic response to the nasal diseases. The correlation among velocity of intranasal flow, pressure drop and deposition ratio, which are main parameters for intranasal transportation of medicinal droplets in the nebulizer treatment, indicates that the basis of the intranasal transportation show similar characteristics in all patient's cases. These results mean that there is an optimum condition of nebulizer treatment for all patients who suffer nasal diseases. Further research of the intranasal transport phenomena for many patient's cases is required to survey the best treatment condition.
Since the development of the medical image processing technique has been in progress, the CFD analysis for human body, such as blood flow from the heart, respiration flow in the pharynx and the lung, will be widely spread and achieve tangible results in clinical practices within the next several years.

7. Acknowledgement

This work was supported by the grant from JSPS KAKENHI 19760114.

8. References

Akiyama, M. (2002). *Analysis of Two-Phase Flow Dynamics: Multi-Physics Flow Analysis*, Korona Inc., Tokyo.

Boyle, R. & Thomas, R. (1988). *Computer Vision: A First Course*, Blackwell Scientific Publications, New York.

Haruna, S. (2003). *An endoscope surgical operation of chronic sinus infection*, Hokendojinsha Inc., Tokyo.

Lindemann, J., Keck, T., Wiesmiller, K., Sander, B., Brambs, H.-J., Rettinger, G. & Pless, D. (2004). A numerical simulation of intranasal air temperature during inspiration, *The Laryngoscope* Vol.114(No.1): 1037–1041.

Lindemann, J., Keck, T., Wiesmiller, K., Sander, B., Brambs, H.-J., Rettinger, G. & Pless, D. (2005). Numerical simulation of intranasal airflow after radical sinus surgery, *American Journal of Otolaryngology* Vol.26(No.1): 175–180.

Lorensen, W. E. & Cline, H. E. (1987). Marching cubes:, *Computer Graphics: A high Resolution 3D Surface Construction Algorithm* Vol.21(No.4): 163–169.

Monya, M., Yamamoto, T., Nakata, S., Nakashima, T., Yamamoto, T. & Suzuki, T. (2009). Cfd analysis for intranasal mass transportation in deviated septum case (japanese), *JSME Journal Series B* Vol.75(No.751): 175–180.

Nakahashi, K. (1995). *Grid Generation and Computer Graphics*, Univ. of Tokyo, Tokyo.

Savitzky, A. & Golay, M. J. E. (1964). Smoothing and differentiation of data by simplified least squares procedures, *Anal. Chem.* Vol.36(No.8): 1627–1639.

Sun, C. (2006). Moving average algrithms for diamond, hexagon, and general polygonal shaped window operation, *Pattern Recognition Letters* Vol.27(No.6): 1627–1639.

Tamura, H. (2002). *Computer Image Processing*, Ohm Inc., Tokyo.

Weinhold, I. & Mlynski, G. (2004). Numerical simulation of air flow in the human nose, *Eur Arch Otorhinolaryngol* Vol.261(No.1): 452–455.

Yamamoto, T., Nakata, S., Nakashima, T. & Yamamoto, T. (2009). Computational fluid dynamics simulation for intranasal flow (japanese), *Foresight of Otorhinolaryngology* Vol.52(No.1): 24–29.

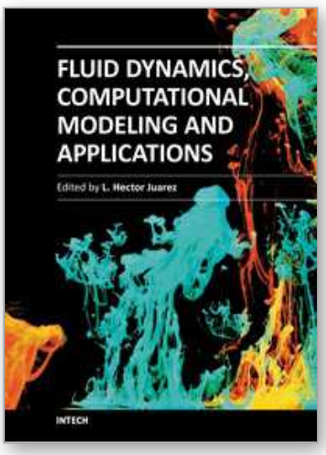

Fluid Dynamics, Computational Modeling and Applications

Edited by Dr. L. Hector Juarez

ISBN 978-953-51-0052-2
Hard cover, 660 pages
Publisher InTech
Published online 24, February, 2012
Published in print edition February, 2012

The content of this book covers several up-to-date topics in fluid dynamics, computational modeling and its applications, and it is intended to serve as a general reference for scientists, engineers, and graduate students. The book is comprised of 30 chapters divided into 5 parts, which include: winds, building and risk prevention; multiphase flow, structures and gases; heat transfer, combustion and energy; medical and biomechanical applications; and other important themes. This book also provides a comprehensive overview of computational fluid dynamics and applications, without excluding experimental and theoretical aspects.

InTech Europe
University Campus STeP Ri
Slavka Krautzeka 83/A
51000 Rijeka, Croatia
Phone: +385 (51) 770 447
Fax: +385 (51) 686 166
www.intechopen.com

InTech China
Unit 405, Office Block, Hotel Equatorial Shanghai
No.65, Yan An Road (West), Shanghai, 200040, China
中国上海市延安西路65号上海国际贵都大饭店办公楼405单元
Phone: +86-21-62489820
Fax: +86-21-62489821

IntechOpen